Control of Spacecraft Occulter Arrays in Multi-Body Regimes

Lindsay D. Millard*
Purdue University, West Lafayette, Indiana, 47907, USA
Kathleen C. Howell†
Purdue University, West Lafayette, Indiana, 47907, USA

Free-flying occulter-telescope arrays may be powerful tools in the study of nearby exosolar planets. The external occulter technique enables significant science goals while requiring relaxed metrology in comparison to interferometric spacecraft arrays. Thus, the National Aeronautics and Space Administration is considering the Terrestrial Planet Finder-Occulter (TPF-O) as a potential precursor to planned interferometric array missions. In this study, several control strategies are developed and implemented on two TPF-O design reference missions. Control methods considered include impulsive maneuvers, nonlinear optimal control (via continuous low-thrust), impulsive geometric control, and linear optimal control (via a time-varying linear quadratic regulator). The strategies are compared based on the total required control effort, robustness to measurement error, and feasibility. All control analysis is performed assuming that the occulter and telescope spacecraft are moving near a Sun-Earth collinear libration point (L_2), and therefore, the spacecraft motion is influenced by the gravitational force of multiple bodies.

I. Nomenclature

t_1	time at initiation of maneuver period
t_2	time at initiation of observation period
$\bar{X}$	state of spacecraft in synodic frame
U	pseudo-potential function
r_1	distance from spacecraft to Sun
r_2	distance from spacecraft to Earth
$\delta\bar{X}$	deviation of state from nominal orbit
μ	non-dimensional mass parameter
$A(t)$	coefficient matrix in linear variational equations of motion in synodic frame
$\Phi(t, t_0)$	state transition matrix
u_j	control effort in the j direction
$\bar{u}$	vector of control effort
δu	perturbation in control effort
$\bar{X}^o(t)$	reference motion

*Post-Doctoral Resesarcher, Purdue University, West Lafayette, Indiana, 47907; Currently: Associate Engineer, RAND Project Air Force, 1776 Main Street, Santa Monica, California; Member AIAA.
†Hsu Lo Professor of Aeronautical and Astronautical Engineering, Purdue University, 701 W. Stadium Ave., West Lafayette, Indiana; Fellow AAS, Associate Fellow AIAA.

$\bar{u}^o$	control effort required to maintain $\bar{X}^o(t)$
$B(t)$	control input matrix in synodic frame
$\bar{r}$	direction to star from telescope in inertial frame
$\bar{v}$	velocity of telescope spacecraft near Lissajous orbit
$\hat{h}_1$	vector perpendicular to both $\bar{v}$ and $\bar{r}$
$\hat{h}_2$	vector perpendicular to both $\hat{h}_1$ and $\bar{r}$
$\delta\bar{Z}(t)$	deviation from nominal orbit in radial-transverse frame
$C(t)$	matrix transforming states between synodic and radial-transverse frame
J_{lqr}	cost function in LQR formulation
Q_z	weighting matrix associated with state deviation in LQR analysis
R_z	weighting matrix associated with control deviation in LQR analysis
$P(t)$	solution to differential Riccati equation for LQR analysis
$S(t)$	solution to transformed differential Riccati equation
G	time transformation matrix
$K(t)$	optimal control gain
$A_z(t)$	coefficient matrix in linear variational equations of motion in radial-transverse frame
B_z	control input matrix in radial-transverse frame
$\delta\bar{y}(t)$	output of feedback linearization algorithm
C_z	constant weighting matrix on output of feedback linearization algorithm
D_z	constant DC gain weighting matrix
$\delta\hat{Z}$	estimate of deviation in state in radial-transverse frame
$F(t)$	coefficient matrix associated with LQG analysis
$G(t)$	coefficient matrix associated with LQG analysis
H	weighting matrix in LQG analysis associated with the DC gain
$\bar{e}_z$	error between measured and actual state in radial-transverse frame
$M(t)$	solution to time-varying Riccati equation in LQG analysis
N_w	weighting matrix in LQG analysis associated with covariance
N_v	weighting matrix in LQG analysis
J_{NL}	cost function in non-linear optimal control formulation
$\bar{\beta}$	weights corresponding to control vector components
H	Hamiltonian
$\bar{\lambda}$	vector of co-states
$E\,(t,0)$	periodic matrix of Floquet eigenvectors
J	Floquet modal matrix
$\bar{z}$	state of spacecraft in Floquet coordinates
T	average period of Lissajous orbit
e_j^*	eigenvalues of Floquet modal matrix
ϵ_j	eigenvalues of monodromy matrix
a_j	real part of Floquet modal matrix eigenvalues
b_j	imaginary part of Floquet modal matrix eigenvalues
$\bar{c}(t)$	coefficients of state deviation expressed in eigenvector basis
$\alpha_i(t)$	coefficients of state deviation in synodic frame basis
Δv	instantaneous change in velocity required for Floquet maneuver
DRM	Design Reference Mission

II. Introduction

STUDIES have revealed free-flying occulter-telescope arrays to be powerful tools in the study of nearby exosolar planets [1, 2]. In 2006, Cash demonstrates that the optical technology required for free-flying occulter-telescope missions has reached a readiness level adequate to locate Earth-like planets in other solar systems [3]. The external occulter technique requires relaxed metrology in comparison to those required by interferometric arrays, such as the Space Interferometry Mission (SIM) and Terrestrial Planet Finder (TPF) [4, 5]. Thus, an occulter-telescope system may achieve many of the NASA Origins science goals while also testing formation-flying concepts and techniques required for future interferometric array missions [6].

Most recently, NASA has considered the Terrestrial Planet Finder-Occulter (TPF-O) as a potential precursor mission to TPF. The TPF-O hardware consists of two spacecraft flying in formation: an occulter and a telescope spacecraft. In 2006, trajectory analysis of a TPF-O mission concept by Lo assumes an occulter formation moving near a Sun-Earth L_2 halo orbit [7]. The occulter-telescope observes 50 to 100 randomly placed stars on the celestial sphere. It is assumed that the control is impulsive and that the occulter is "drifting" during the observation periods. Lo concludes that the "drifting" assumption precludes mission requirements, as the occulter does not remain within a specified positioning tolerance during observation periods. Lo also suggests that occulter-telescope designs may be useful for locating Jupiter-like planets, but the control cost may be prohibitively large to search for smaller Earth-like planets. In 2007, Vanderbei, Cady, and Kasdin, investigate the optimal occulter design in a search for Earth-like planets [8]. Occulters, of different sizes, located between 18,000 km and 100,000 km from a telescope spacecraft are used successfully to locate Earth-like planets. Also in 2007, a high-level analysis for the TPF-O formation-flying design is published by Leitner [9]. Leitner suggests that several trade studies should be undertaken to determine the type of control (impulsive, low-thrust, or hybrid), as well as the type of control algorithm, best suited for the mission. Most recently, Millard and Howell explore several control strategies for TPF-O mission concepts [10]. This study expands on the work of Millard and Howell.

III. Terrestrial Planet Finder - Occulter Mission Concept

The focus of the NASA Terrestrial Planet Finder-Occulter (TPF-O) mission is a search for Earth-like planets in other solar systems via an optical formation of spacecraft. The formation is comprised of two spacecraft: one telescope spacecraft and one occulter spacecraft. The telescope spacecraft moves near a nominal Sun-Earth L_2 Lissajous orbit. During an observation period, the telescope and the occulter align along a specified inertial direction to a star of interest. The two spacecraft are required to maintain a fixed relative distance during this phase to image the planet effectively. During the transit, or maneuver, period there is no constraint on the geometry of the occulter and telescope. During the transit period, the spacecraft in the formation are re-configuring to point toward a different star of interest. The "transit period" refers to the time period between t_1 and t_2, while the "observation period" denotes the time interval between t_2 and t_3, as illustrated in Figure 1.

Over the duration of the mission, the path of the occulter is dictated by a star sequence. This star sequence represents a list of stars that are in the same spectral class as the Sun, indicating a higher potential for the existence of nearby, orbiting Earth-like planets. The required observation time at each star and the specific length of time allotted for maneuvering between each observation is also included in the star sequence. In this analysis, two star sequences, denoted as Design Reference Missions (DRM), are used for comparison: DRM 4 and DRM 5. These sequences are specified as options for TPF-O, as defined by NASA Goddard Space Flight Center. The general characteristics of the star sequences are compared in Table 1. In general, the transit and observation times in DRM 4 are shorter than those in DRM 5. Also, the occulter is placed significantly closer to the telescope spacecraft in DRM 5. Placement of the stars, in a given sequence

Table 1. The TPF-O Mission analysis encompasses design reference missions 4 and 5, and the associated star sequences.

Star Sequence	Mission Duration	Number of Observations	Distance to Occulter	Average Observation	Average Transit
DRM4	1832 days	134	72000 km	2.67 days	10.99 days
DRM5	1840 days	102	37800 km	3.24 days	14.80 days

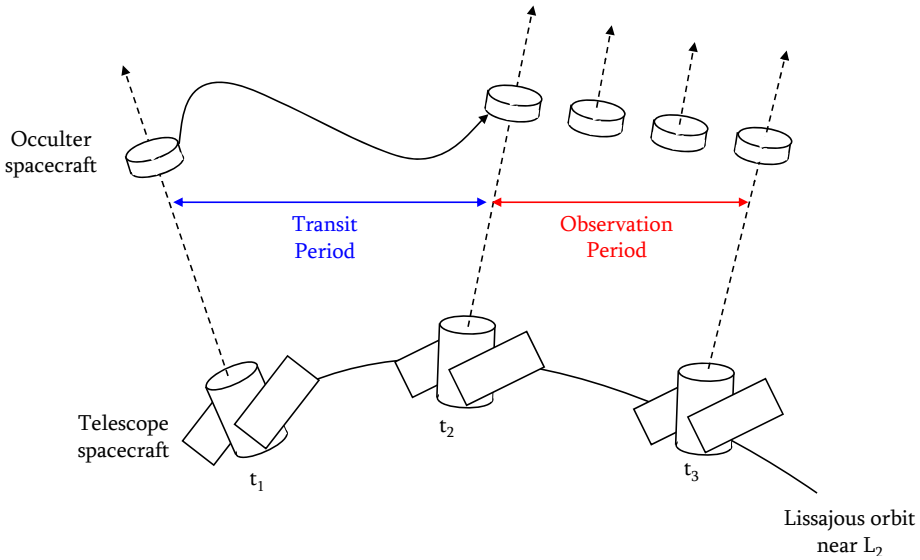

Figure 1. A schematic of the TPF-O mission shows observation and transit periods.

on a celestial sphere, is noted in Figure 2.

In this analysis, the reference trajectory is a Lissajous orbit, or quasi-periodic orbit, near L_2. This particular orbit was identified by NASA Goddard Space Flight Center as a possibly advantageous orbit for the TPF-O mission, and appears in Figure 3.

IV. Dynamic Model: Circular Restricted Three-Body Problem

The motion of a spacecraft in the circular restricted three-body problem (CR3BP) is described in terms of rotating coordinates relative to the barycenter of the system primaries. For this analysis, emphasis is placed on formations near the libration points in the Sun-Earth/Moon system. Thus, the rotating x-axis is directed from the Sun toward the Earth/Moon barycenter. The z-axis is normal to the plane of motion of the primaries, and the y-axis completes the right handed triad. The system is represented in Figure 4.

Let $\bar{X} = \begin{bmatrix} x & y & z & \dot{x} & \dot{y} & \dot{z} \end{bmatrix}$, then the general non-dimensional equations of motion of a spacecraft, relative to the system barycenter, are,

$$\ddot{x} - 2\dot{y} - x = -\frac{(1-\mu)(x+\mu)}{r_1^3} - \frac{\mu(x-(x-\mu))}{r_2^3} \tag{1}$$

$$\ddot{y} + 2\dot{x} - y = -\frac{(1-\mu)y}{r_1^3} - \frac{\mu y}{r_2^3} \tag{2}$$

$$\ddot{z} = -\frac{(1-\mu)z}{r_1^3} - \frac{\mu z}{r_2^3} \tag{3}$$

where

$$r_1 = \left((x+\mu)^2 + y^2 + z^2\right)^{1/2} \tag{4}$$

$$r_2 = \left((x-(1-\mu))^2 + y^2 + z^2\right)^{1/2} \tag{5}$$

The quantity μ is a non-dimensional mass parameter associated with the system. For the Sun-Earth/Moon system, $\mu = 3.0404 \times 10^{-6}$.

A more compact notation incorporates a pseudo-potential function, U, such that,

$$U = \frac{(1-\mu)}{r_1} + \frac{\mu}{r_2} + \frac{1}{2}\left(x^2 + y^2\right) \tag{6}$$

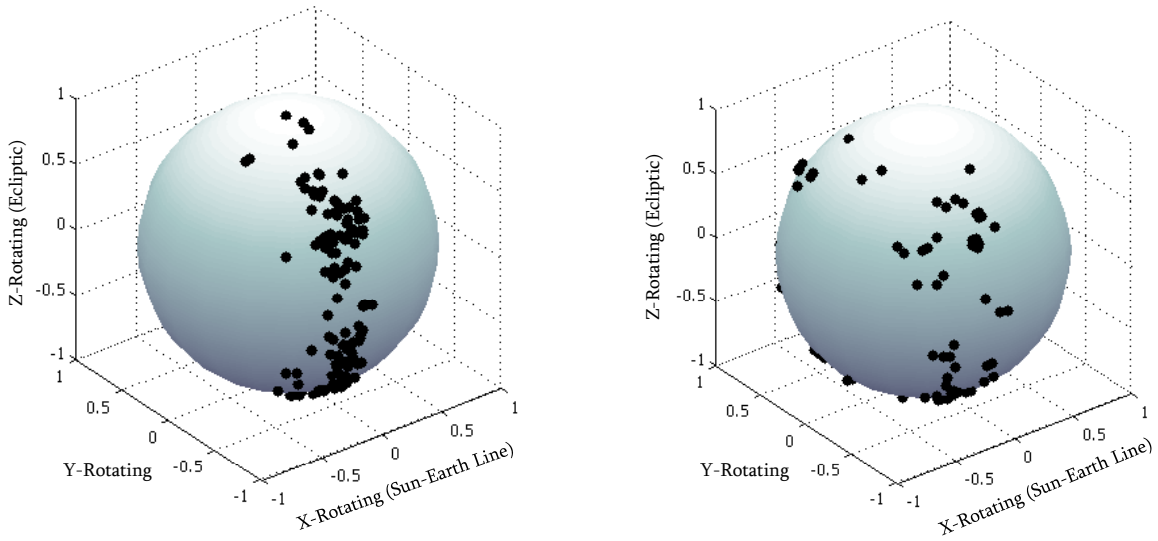

Figure 2. The star sequences for TPF-O DRM 4 and DRM 5 are shown on the celestial sphere.

Then, the scalar equations of motion are rewritten in the form,

$$\ddot{x} = U_x + 2\dot{y} = f_x\left(x, \dot{x}, y, \dot{y}, z, \dot{z}\right) \tag{7}$$

$$\ddot{y} = U_y - 2\dot{x} = f_x\left(x, \dot{x}, y, \dot{y}, z, \dot{z}\right) \tag{8}$$

$$\ddot{z} = U_z = f_z\left(x, \dot{x}, y, \dot{y}, z, \dot{z}\right) \tag{9}$$

where the symbol U_j denotes the partial derivative of U with respect to X_j. Equations (1)-(3) or equations (7)-(9) comprise the dynamic model in the circular restricted three-body problem.

Given a solution to the nonlinear differential equations, linear variational equations of motion in the CR3BP can be derived in matrix form as,

$$\delta\dot{\bar{X}}(t) = A(t)\delta\bar{X}(t) \tag{10}$$

where $\delta\bar{X} = \begin{bmatrix} \delta x & \delta y & \delta z & \delta\dot{x} & \delta\dot{y} & \delta\dot{z} \end{bmatrix}^T$ represents variations with respect to a reference trajectory. Generally, the reference solution of interest is not constant. In this analysis, the reference trajectory is a Lissajous orbit, or a quasi-periodic orbit, near L_2.

For the nominal Lissajous orbit, $A(t)$ is time-varying and of the form,

$$A(t) = \begin{bmatrix} 0 & 0 & 0 & 1 & 0 & 0 \\ 0 & 0 & 0 & 0 & 1 & 0 \\ 0 & 0 & 0 & 0 & 0 & 1 \\ U_{xx} & U_{xy} & U_{yz} & 0 & 2 & 0 \\ U_{yx} & U_{yy} & U_{yx} & -2 & 0 & 0 \\ U_{zx} & U_{zy} & U_{zz} & 0 & 0 & 0 \end{bmatrix} \tag{11}$$

The partials U_{kl} are also functions of time, although the functional dependence on time, t, has been dropped.

The general form of the solution to the system in equation (10) is,

$$\delta\bar{X}(t) = \Phi\left(t, t_0\right)\delta\bar{X}\left(t_0\right) \tag{12}$$

where $\Phi\left(t, t_0\right)$ is the state transition matrix (STM). The STM is a linear map from the initial state at the initial time, t_0, to a state at some later time, t, and thus offers an approximation for the impact of the variations in the initial state on the evolution of the trajectory. The STM must satisfy the matrix differential equation,

$$\dot{\Phi}\left(t, t_0\right) = A(t)\Phi\left(t, t_0\right) \tag{13}$$

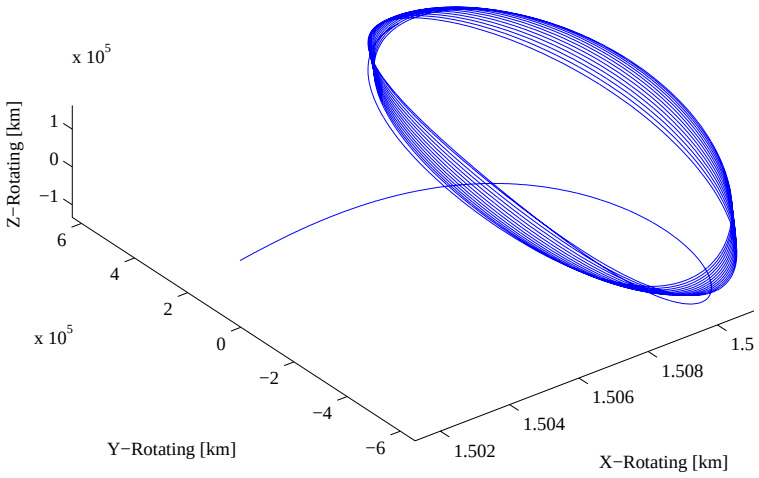

Figure 3. The reference trajectory for the TPF-O Mission is a Lissajous orbit near the Sun-Earth L_2 point.

given the initial condition,

$$\Phi(t, t_0) = I_{6\times 6} \tag{14}$$

where $I_{6\times 6}$ is the 6×6 identity matrix.

The STM at time t can be numerically determined by integrating equation (12) from the initial value. Since the STM is a 6×6 matrix, propagation of equation (12) requires the integration of 36 first-order, scalar differential equations. Because the elements of $A(t)$ depend on the reference trajectory, equation (12) must be integrated simultaneously with the nonlinear equations of motion to generate reference states. This requirement necessitates the integration of an additional 6 first-order equations, for a total of 42 differential equations.

V. Derivation of Control Methods

Optimal nonlinear control as well as geometric control methods are compared to more traditional linear quadratic regulators and feedback linearization. The control strategies are implemented and evaluated for the TPF-O mission concept.

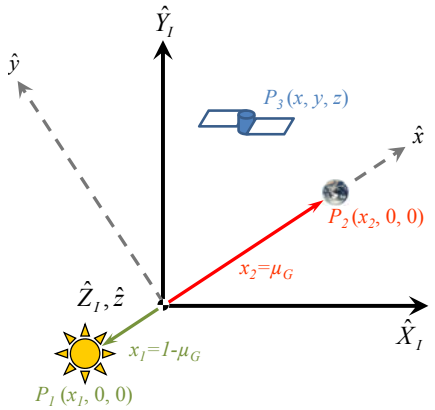

Figure 4. Inertial and rotating frames as defined in the three-body problem.

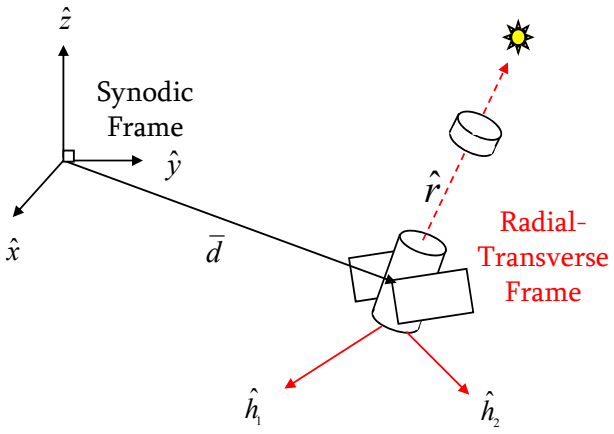

Figure 5. The radial and transverse directions are defined within the TPF-O mission concept.

V.A. TPF-O: Time-Varying LQR Control

Let the motion of a spacecraft moving in the CR3BP be described by,

$$\ddot{x} = f_x\left(x, \dot{x}, y, \dot{y}, z, \dot{z}\right) + u_x \tag{15}$$
$$\ddot{y} = f_y\left(x, \dot{x}, y, \dot{y}, z, \dot{z}\right) + u_y \tag{16}$$
$$\ddot{z} = f_z\left(x, \dot{x}, y, \dot{y}, z, \dot{z}\right) + u_z \tag{17}$$

where f_x, f_y, and f_z are defined in equations (7)-(9) and $\bar{u}(t) = \begin{bmatrix} u_x & u_y & u_z \end{bmatrix}^T$ is an applied control (acceleration) vector. Let $\bar{X}^o(t)$ represent some reference motion that satisfies the system equations (15)-(17) and, then, $\bar{u}^o(t)$ denotes the control effort required to maintain $\bar{X}^o(t)$. Linearization about this reference solution yields a system of the form,

$$\delta\dot{\bar{X}}(t) = A(t)\delta\bar{X} + B(t)\delta\bar{u}(t) \tag{18}$$

where $\delta\bar{X}(t)$ and $\delta\bar{u}(t)$ represent perturbations relative to $\bar{X}^o$ and $\bar{u}^o(t)$, respectively. The matrix $A(t)$ is defined in equation (11) and $B(t) = B = \begin{bmatrix} 0_{3\times3} & I_{3\times3} \end{bmatrix}^T$. The matrix $B(t)$ is selected such that the control input can instantaneously change only the velocity of the satellite (not position).

For the TPF-O mission, the tolerances for the position of the occulter spacecraft are specified in terms of a radial and transverse component. The radial direction is defined as the direction from the telescope to the target star, as illustrated in Figure 5. The transverse directions lay anywhere in a plane perpendicular to this radial direction. The occulter is constrained to remain within ±100km of the baseline path in the radial direction and ±10m from the baseline position in the transverse direction. Because the dynamics of the system are expressed in a rotating coordinate frame, it is difficult to determine the effect of varying control on the precision in the radial and transverse directions.

To add insight to the analysis, the LQR problem is formulated in terms of radial and transverse coordinates. Let the direction to the star target from the telescope be defined in the synodic frame as $\bar{r} = r_1\hat{x} + r_2\hat{y} + r_3\hat{z}$ and the direction of the velocity of the telescope in the vicinity of the Lissajous orbit be defined as $\bar{v} = v_1\hat{x} + v_2\hat{y} + v_3\hat{z}$. Then, a vector perpendicular to both $\bar{r}$ and $\bar{v}$ is,

$$[h]\hat{h}_1 = \frac{\bar{r} \times \bar{v}}{||\bar{r} \times \bar{v}||} \tag{19}$$

The direction $\hat{h}_1$ is defined as the first transverse direction. This choice is arbitrary, since the specific orientation of the transverse coordinate does not effect the problem formulation. The new coordinate frame is completed by $\hat{h}_2$ such that,

$$\hat{h}_2 = \frac{\bar{r}}{||\bar{r}||} \times \hat{h}_1 \tag{20}$$

To transform the linearized system in equation (18) into the new coordinate frame, a transformation matrix, $C(t)$, is derived. This matrix transforms the perturbations $\delta\bar{X}(t)$ to the new coordinate system, that is, $\delta\bar{Z}(t) = \begin{bmatrix} r & h_1 & h_2 & \dot{r} & \dot{h}_1 & \dot{h}_2 \end{bmatrix}^T$ such that,

$$\delta\bar{X}(t) = C(t)\delta\bar{Z}(t) \tag{21}$$

$$\delta\dot{\bar{X}}(t) = C(t)\delta\dot{\bar{Z}}(t) + \dot{C}(t)\delta\bar{Z}(t) \tag{22}$$

Substituting equations (21) and (22) into equation (18) yields,

$$\delta\dot{\bar{Z}}(t) = \left[C(t)^{-1}A(t)C(t) - C(t)^{-1}\dot{C}(t)\right]\delta\bar{Z}(t) + C(t)^{-1}B\delta\bar{u}(t) \tag{23}$$

To minimize some combination of the error state and required control, Bryson and Ho employ a quadratic cost function,

$$\min J_{LQR} = \frac{1}{2}\int_{t_0}^{t_f}\left(\delta\bar{Z}(t)^T Q_z \delta\bar{Z}(t) + \delta\bar{u}(t)^T R_z \delta\bar{u}(t)\right)dt \tag{24}$$

subject to the governing state equations (23) with initial conditions $\delta\bar{X}\left(t_0\right) = \delta\bar{X}_0$. The matrices Q_z and R_z represent the weighting on the radial and transverse state error and control effort, respectively. In this analysis, weighting matrices,

$$Q_z = I_{6\times 6} \tag{25}$$

$$R_z = diag\begin{bmatrix} 10^{-5} & 10^{-10} & 10^{-10} \end{bmatrix} \tag{26}$$

are sufficient in almost all cases to maintain the desired tolerances on the state. However, recall that only the relative magnitudes of Q_z and R_z are significant. Both are positive definite. Because the individual state errors are decoupled from the required control, Q_z and R_z are both diagonal matrices.

Application of the Euler-Lagrange theorem to the system in equations (23) and (24) yields the following optimality requirement on the control variable,

$$\delta\bar{u}(t) = -R_z^{-1}C(t)^{-1}BP(t)\delta\bar{Z}(t) \tag{27}$$

where $P(t)$ is a solution of the matrix differential Riccati equation,

$$\begin{aligned}\dot{P}(t) = &-\left[C(t)^{-1}A(t)C(t) - C(t)^{-1}\dot{C}(t)\right]^T P(t) - P(t)\left[C(t)^{-1}A(t)C(t)\right.\\ &\left.-C(t)^{-1}\dot{C}(t)\right] + P(t)C(t)^{-1}BR_z^{-1}\left[C(t)^{-1}B\right]^T P(t) - Q_z\end{aligned} \tag{28}$$

subject to $P(t_f) = [0_{6\times 6}]$.

Equations (23) and (28) represent a two-point boundary value problem with 42 first-order, ordinary differential equations. However, for application to the CR3BP, this complexity can be avoided by exploiting the time invariance properties associated with the dynamical model. Howell and Marchand [11] develop a time transformation,

$$P\left(t_f - t\right) = G^{-1}S(t)G \tag{29}$$

where $G_{jj} = (-1)^{j-1}$, that enables simple forward integration to numerically solve a transformed Riccati matrix differential equation,

$$\begin{aligned}\dot{S}(t) = &-\left[C(t)^{-1}A(t)C(t) - C(t)^{-1}\dot{C}(t)\right]^T S(t) - S(t)\left[C(t)^{-1}A(t)C(t)\right.\\ &\left.-C(t)^{-1}\dot{C}(t)\right] - S(t)C(t)^{-1}BR_z^{-1}\left[C(t)^{-1}B\right]^T S(t) + G^{-1}Q_z G\end{aligned} \tag{30}$$

Thus, the resulting optimal gain is defined as,

$$K\left(t_f - t\right) = -R_z^{-1}\left[C(t)^{-1}B\right]^T S(t)G \tag{31}$$

and can be implemented at each numerical time step. The system of equations in (23) and the matrix differential equation in (30) are numerically integrated forward in time, subject to $\bar{X}(t_0) = \bar{X}^o(t_0)$ and $S(t_0) = 0$, respectively. Simultaneously, an optimal gain matrix is calculated at each integration time step and control is applied to the perturbed spacecraft motion.

It is notable that nearly the same optimal control gains can be computed by solving the algebraic Riccati equation at each integration step, rather than numerically integrating the differential Riccati equation. This method, although arguably less rigorous, requires far less computation time and, therefore, is very useful for preliminary analysis. Also, if the reference trajectory is periodic or well known a priori, the gain matrix can be computed and stored as a function of time for later implementation. If the integration time steps are defined such that no interpolation of $K(t)$ is necessary, computation time can be greatly reduced.

V.B. TPF-O: Time-Varying LQG Control

To facilitate error analysis, a linear quadratic Gaussian (LQG) method is employed. The actual system may be represented as,

$$\delta\dot{\bar{Z}}(t) = A_z(t)\delta\bar{Z}(t) + B_z\delta\bar{u}(t) \tag{32}$$

$$\delta\bar{y}(t) = C_z\delta\bar{Z}(t) + D_z\delta\bar{u}(t) \tag{33}$$

where $\delta\bar{Z}(t)$ represents the perturbations of the occulter spacecraft in the radial-transverse frame, $A_z = C(t)^{-1}A(t)C(t) - C(t)^{-1}\dot{C}(t)$, and $B_z = C(t)^{-1}B$, as defined in equation (23). Equation (33) represents the output of the time-varying linear system. In this formulation, full state feedback is assumed, thus, $C_z(t) = C_z = I_{6\times6}$ and $D_z = 0_{6\times3}$. Given a measurement of the output of the state, $\delta\bar{y}(t)$, an estimate of the state, $\delta\hat{Z}(t)$ may be defined as,

$$\delta\dot{\hat{Z}}(t) = F(t)\delta\hat{Z}(t) + G(t)\delta\bar{y}(t) + H\delta\bar{u}(t). \tag{34}$$

A control gain is derived based on the value of the measured state, $\delta\hat{Z}(t)$, rather than the actual state, $\delta\bar{Z}(t)$, such that

$$\delta\bar{u}(t) = -K(t)\delta\hat{Z}(t) \tag{35}$$

where $K(t) = -R_z^{-1}\left[C(t)^{-1}B\right]^T S(t)G$, as defined in equation (31) is selected to create a desired response in the actual system. To determine a desirable $K(t)$, the error between the actual state and estimated state must approach zero. The error system is,

$$\bar{e}_z(t) = \delta\bar{Z}(t) - \delta\hat{Z}(t) \tag{36}$$

$$\begin{aligned}\dot{\bar{e}}_z(t) &= \delta\dot{\bar{Z}}(t) - \delta\dot{\hat{Z}}(t) \\ &= A_z(t)\delta\bar{Z}(t) + B_z\delta\bar{u}(t) - F\delta\hat{Z}(t) - G(t)\delta\bar{y}(t) - H\delta\bar{u}(t).\end{aligned} \tag{37}$$

By substituting equation (33) and rearranging terms, the error system becomes,

$$\dot{\bar{e}}(t) = \left(A_z(t) - G(t)C_z\right)\bar{e}_z(t) - F\hat{Z}(t) + \left(B_z - G(t)D_z - H\right)\delta\bar{u}(t). \tag{38}$$

Finally, an appropriate choice for the matrices $F_z(t)$ and H_z,

$$F(t) = A_z(t) - G(t)C_z \tag{39}$$

$$H(t) = B_z - G(t)D_z \tag{40}$$

simplifies the system to,

$$\dot{\bar{e}}_z(t) = \left(A_z(t) - G(t)C_z\right)\bar{e}_z(t). \tag{41}$$

Thus, the error system will converge if $G(t)$ is selected such that $A_z(t) - G(t)C_z$ is asymptotically stable. However, the best estimate of the actual state is a selection of $G(t)$ based on the solution to a time-varying Riccati equation,

$$\dot{M}(t) = M(t)A_z^T(t) + A_z(t)M(t) + B_zN_wB_z^T - M(t)C_z^TN_v^{-1}C_zM(t) \tag{42}$$

$$G(t) = M(t)C_z^TN_v^{-1} \tag{43}$$

where N_w and N_v are weights used in the optimization process. To determine both the desired control gain, $K_z(t)$, the desired state estimation gain, G_z, and the value of the state at each point in time, a system of 48 differential equations is numerically integrated,

$$\begin{bmatrix} \delta\dot{\bar{Z}}(t) \\ \dot{\bar{e}}_z(t) \end{bmatrix} = \begin{bmatrix} A_z(t) - B_z K(t) & B_z K(t) \\ 0 & A_z(t) - G(t)C_z \end{bmatrix} \begin{bmatrix} \delta\bar{Z}(t) \\ \bar{e}(t) \end{bmatrix} \tag{44}$$

At each integration step, an algebraic solution to the Riccati equation is used to estimate the value of $K(t)$ and $G(t)$.

V.C. TPF-O: Nonlinear Optimal Control

To determine minimum fuel maneuvers for a spacecraft moving in the full nonlinear CR3BP, a traditional nonlinear optimal control problem is formulated. Let a cost function be defined as,

$$\min J_{NL} = \int_0^{t_f} \left(\beta_x u_x^2 + \beta_y^2 u_y^2 + \beta_z u_z^2\right) dt \tag{45}$$

where the vector $\bar{\beta} = \begin{bmatrix} \beta_x & \beta_y & \beta_z \end{bmatrix}^T$ is comprised of the weights on the corresponding control vector components, u_x, u_y, and u_z. The Hamiltonian is then represented by,

$$H = \beta_x u_x^2 + \beta_y u_y^2 + \beta_z u_z^2 + \lambda_1 \dot{x} + \lambda_2 \dot{y} + \lambda_3 \dot{z} + \lambda_4 \ddot{x} + \lambda_5 \ddot{y} + \lambda_6 \ddot{z} \tag{46}$$

where $\bar{\lambda}(t) = \begin{bmatrix} \lambda_1 & \lambda_2 & \lambda_3 & \lambda_4 & \lambda_5 & \lambda_6 \end{bmatrix}^T$ is a vector of co-states. The Euler equations are derived via the partial derivative of the Hamiltonian with respect to the state, as follows,

$$\dot{\lambda}_1 = -\frac{\partial H}{\partial x} = -\lambda_4 \frac{\partial}{\partial x}(\ddot{x}) - \lambda_5 \frac{\partial}{\partial x}(\ddot{y}) - \lambda_6 \frac{\partial}{\partial x}(\ddot{z}) \tag{47}$$

$$\dot{\lambda}_2 = -\frac{\partial H}{\partial y} = -\lambda_4 \frac{\partial}{\partial y}(\ddot{x}) - \lambda_5 \frac{\partial}{\partial y}(\ddot{y}) - \lambda_6 \frac{\partial}{\partial y}(\ddot{z}) \tag{48}$$

$$\dot{\lambda}_3 = -\frac{\partial H}{\partial z} = -\lambda_4 \frac{\partial}{\partial z}(\ddot{x}) - \lambda_5 \frac{\partial}{\partial z}(\ddot{y}) - \lambda_6 \frac{\partial}{\partial z}(\ddot{z}) \tag{49}$$

$$\dot{\lambda}_4 = \frac{\partial H}{\partial \dot{x}} = -\lambda_1 + 2\lambda_5 \tag{50}$$

$$\dot{\lambda}_5 = \frac{\partial H}{\partial \dot{y}} = -\lambda_2 + 2\lambda_4 \tag{51}$$

$$\dot{\lambda}_6 = \frac{\partial H}{\partial \dot{z}} = -\lambda_3 \tag{52}$$

Then, the conditions for optimality become,

$$\frac{\partial H}{\partial u_x} = 2\beta_x u_x + \lambda_4 = 0 \tag{53}$$

$$\frac{\partial H}{\partial u_y} = 2\beta_y u_y + \lambda_5 = 0 \tag{54}$$

$$\frac{\partial H}{\partial u_z} = 2\beta_z u_z + \lambda_6 = 0 \tag{55}$$

This control strategy is implemented to maneuver a spacecraft from a specified initial state (both position and velocity) to a specified final position. Therefore, the boundary conditions include three "free" final conditions on both the state and co-state variables,

$$\bar{X}(0) = \begin{bmatrix} x_0 & y_0 & z_0 & \dot{x}_0 & \dot{y}_0 & \dot{z}_0 \end{bmatrix} \tag{56}$$

$$\bar{X}(t_f) = \begin{bmatrix} x_f & y_f & z_f & free & free & free \end{bmatrix} \tag{57}$$

$$\bar{\lambda}(t_f) = \begin{bmatrix} free & free & free & 0 & 0 & 0 \end{bmatrix} \tag{58}$$

The two-point boundary value problem is solved using a function (bvp4c) available in the Matlab Optimization Toolbox ®. Final conditions for the "free" state and co-state elements are determined based upon knowledge of the optimal LQR solution for the same maneuver.

V.D. Impulsive Control via Differential Corrections

The use of a differential corrector is arguably the simplest method for computation of the required impulsive velocity change to reach a specified future position. An impulsive velocity change is also, potentially, the easiest to implement using available chemical thrusters. While LQR, IFL, and nonlinear methods may reveal advantageous trajectories that require less fuel, these approaches may be significantly more complicated to execute. It may be necessary to discretize and optimize the control results to employ common propulsion systems.

V.E. TPF-O: Floquet Control

A version of Floquet's Theorem appears in Perko [12]:

> If $A(t)$ is a continuous T-periodic matrix, then for all t any fundamental matrix solution for equation (10) can be written in the form
>
> $$\Phi(t,0) = E(t,0)e^{Jt} \tag{59}$$
>
> where $E(t,0)$ is a nonsingular, differentiable, T-periodic matrix and J is a constant matrix. Furthermore, if $\Phi(0,0) = I$ then $E(0,0) = I$.

Under the hypothesis of Floquet's Theorem, the nonautonomous linear system of equations (10), under the linear change of coordinates

$$\bar{z}(t) = E^{-1}(t,0)\delta\bar{X}(t) \tag{60}$$

reduces to the autonomous linear system

$$\dot{\bar{z}}(t) = J\bar{z}(t). \tag{61}$$

Thus, if $A(t)$ is evaluated along a halo orbit, the constant matrix J contains all of the relevant stability information associated with the periodic orbit, in the linearized sense.

The matrix J in equation (59) is not unique. From Floquet's Theorem, the monodromy matrix may be written as,

$$\Phi(T,0) = E(T,0)e^{JT} \tag{62}$$

and, since $E(t,0)$ is periodic with period T,

$$\begin{aligned}\Phi(T,0) =& E(0,0)e^{JT} \\ =& e^{JT}\end{aligned} \tag{63}$$

Denote the eigenvalues of E, which may be complex, as $e_j^* = a_j + ib_j$. These eigenvalues are termed the characteristic exponents, or *Poincaré exponents* and ultimately determine orbital stability. The eigenvalues of the monodromy matrix, ϵ_j, are related to the Poincaré exponents as follows,

Table 2. Poincaré exponents are related to the eigenvalues of the monodromy matrix; ϵ_j provide stability information about the associated periodic orbit.

Subspace	Characteristic Exponent $e_j^* = a_j + ib_j$	Characteristic Multiplier $\epsilon_j = \exp\left(e_j^* T\right)$
Unstable	$a_j > 0$	$\|\|\epsilon_j\|\| > 1$
Center	$a_j = 0$	$\|\|\epsilon_j\|\| = 1$
Stable	$a_j < 0$	$\|\|\epsilon_j\|\| < 1$

$$\epsilon_j = \exp\left(e_j^* T\right) \tag{64}$$

Thus, the characteristic exponents are also written as $e_j^* = \frac{1}{T}\ln\epsilon_j$. The real part of the characteristic exponents, a_j, determine the magnitudes of the characteristic multipliers, $||\epsilon_j|| = e^{a_j T}$, as well as the stability properties of the orbit. This stability information is summarized in Table (2) from [13].

Many halo orbits are inherently unstable. In fact, the six-dimensional eigenstructure of the associated monodromy matrix is characterized by one unstable eigenvalue (ϵ_1), one unstable eigenvalue (ϵ_2), and four eigenvalues in the center subspace. Two of these neutrally stable eigenvalues are located on the unit circle (ϵ_3 and ϵ_4) and the remaining two are exactly equal to one (ϵ_5 and ϵ_6). Thus, the eigenvalues appear as reciprocal pairs. This specific eigenstructure results from the periodicity of the associated reference orbit.

The characteristics of the phase space can be exploited to decompose any variation relative to the orbit into components in the three subspaces. At any point in time, the vector perturbation $\delta\bar{X}(t)$ can be expressed in terms of any six-dimensional basis. The eigenvectors of the state transition matrix at time t, ($\bar{e}_i(t)$), are defined by the columns of $E(t,0)$ and form a non-orthogonal six-dimensional basis. Hence,

$$\delta\bar{X}(t) = \sum_{i=1}^{6} \delta\bar{X}_i(t) = \sum_{i=1}^{6} c_i(t)\bar{e}_i(t) \tag{65}$$

where $\delta\bar{X}_i(t)$ denotes the component of $\delta\bar{X}(t)$ along the i^{th} mode, $\bar{e}_i(t)$, and the coefficients $c_i(t)$ are defined as the elements of the vector $\bar{c}(t)$ determined as,

$$\bar{c}(t) = E(0,t)^{-1}\delta\bar{X}(t) \tag{66}$$

If the orbit is perturbed only in the direction of the center modes, the resulting trajectory will be quasi-periodic, i.e., it will remain bounded to the reference halo orbit over extended periods of time.

Floquet analysis is applied to keep an occulter-telescope formation within the center subspace during the transit periods. Several small maneuvers are performed to maintain the spacecraft state near the center subspace of the reference Lissajous orbit.

A Floquet structure is implemented by Gómez et al.[14], and later by Howell and Keeter [15] , as the basis of a station-keeping strategy for a single spacecraft evolving along a halo orbit. Both investigations determine the impulsive maneuver scheme that is required to remove the component, $\delta\bar{X}_1$, of the complete perturbation, $\delta\bar{X}(t)$, in the direction of the unstable mode at discrete intervals. For instance, if,

$$\delta\bar{X}_{desired}(t) = \sum_{i=2}^{6} \left(1 + \alpha_i(t)\right)\delta\bar{X}_i(t) \tag{67}$$

denotes the desired perturbation relative to the reference orbit, then $\bar{\alpha}(t)$ is some, yet to be determined, coefficient vector. Note that the limits of the summation range from 2 through 6 in recognition of the fact that the perturbation in the direction of the unstable mode, ϵ_1, has been removed. The linearized control problem then reduces to computing the impulsive maneuver, $\Delta\bar{v}(t)$, such that,

$$\sum_{i=2}^{6} \left(1 + \alpha_i(t)\right)\delta\bar{X}_i(t) = \sum_{k=1}^{6} \delta\bar{X}_k(t) + \begin{bmatrix} 0_{3\times1} \\ \Delta\bar{v}(t)_{3\times1} \end{bmatrix}. \tag{68}$$

After some reduction, equation (68) can be rewritten in matrix form as,

$$\left[\begin{array}{ccccc|c} \delta\bar{X}_2(t) & \delta\bar{X}_3(t) & \delta\bar{X}_4(t) & \delta\bar{X}_5(t) & \delta\bar{X}_6(t) & \begin{array}{c}0_{3\times3}\\ I_{3\times3}\end{array} \end{array}\right] \times \left[\begin{array}{c} \bar{\alpha}(t)_{5\times1} \\ \Delta\bar{v}(t)_{3\times3} \end{array}\right] = \delta\bar{X}_1(t) \tag{69}$$

where $\bar{\alpha}$ represents a 5×1 vector formed by the α_j components in equation (67). Therefore, the maneuver, $\Delta\bar{v}_{3\times1}$, that is required to remove the unstable mode from the perturbation at any given time can be approximated from equation (69). Howell and Keeter identify this required $\Delta\bar{v}_{3\times1}$ via a minimum norm solution. If the maneuver is constrained to the Sun-Earth line ($\hat{x}$- direction), $\Delta\bar{v}_{1\times1}$ is actually a scalar, and the system possesses an exact solution.

Removal of specific modes beyond simply $\delta\bar{X}_1$ is also possible. If exactly three modes are removed and control is possible in three directions, the system also possesses an exact solution. For example, Marchand and Howell [16] compute the impulsive maneuver $\Delta\bar{v}(t)_{3\times1}$ that is required to remove the portion of the perturbation along modes $\bar{e}_1$, $\bar{e}_3$, and $\bar{e}_4$. It can be determined exactly from the following,

$$\begin{aligned}\left[\begin{array}{c} \bar{\alpha}(t)_{3\times1} \\ \Delta\bar{v}(t)_{3\times1} \end{array}\right] &= \left[\begin{array}{ccc|c} \delta\bar{X}_2(t) & \delta\bar{X}_5(t) & \delta\bar{X}_6(t) & \begin{array}{c}0_{3\times3}\\ -I_{3\times3}\end{array} \end{array}\right]^{-1} \\ &\times \left(\delta\bar{X}_1(t) + \delta\bar{X}_3(t) + \delta\bar{X}_4(t)\right). \end{aligned} \tag{70}$$

Similarly, the $\Delta\bar{v}_{3\times1}$ vector to remove modes $\bar{e}_1$, $\bar{e}_5$, and $\bar{e}_6$ is exactly determined from

$$\begin{aligned}\left[\begin{array}{c} \bar{\alpha}(t)_{3\times1} \\ \Delta\bar{v}(t)_{3\times1} \end{array}\right] &= \left[\begin{array}{ccc|c} \delta\bar{X}_2(t) & \delta\bar{X}_3(t) & \delta\bar{X}_4(t) & \begin{array}{c}0_{3\times3}\\ -I_{3\times3}\end{array} \end{array}\right]^{-1} \\ &\times \left(\delta\bar{X}_1(t) + \delta\bar{X}_5(t) + \delta\bar{X}_6(t)\right). \end{aligned} \tag{71}$$

As formulated in equations (70) and (71), $\Delta\bar{v}(t)_{3\times1}$ is the impulsive control necessary at a given time to remove perturbations in the direction of one unstable mode and two semi-stable modes in the linearized system represented in equation (10). Specifically, the $\Delta\bar{v}_{3\times1}$ indicated in equation (71), is implemented at varying time intervals during the transit period. Because the Lissajous orbit is not perfectly periodic, a similar halo orbit is used to approximate the surrounding phase space while calculating the required velocity change.

Because the spacecraft should eventually reach a specified observation state (which may or may not be in the center subspace) an impulsive targeting maneuver is required at some point during the transit period. This maneuver is added at the time when the smallest total amount of thrust is required to move to the desired observation location. A schematic of the geometric control method, as applied to the TPF-O mission, appears in Figures 6 and 7.

The blue line in Figures 6 and 7 indicates the distance between the path of the spacecraft and the nominal Lissajous orbit in the rotating $\hat{x}$-direction during one transit period (approximately 16 days). A small maneuver is applied at each blue star to successfully maintain the spacecraft state near the center manifold during the transit period. Over longer periods of time, this trajectory is quasi-periodic. The red line in the Figures 6 and 7 represents the path of the spacecraft if no maneuver is implemented. In Figure 7, a point along the center manifold has been identified that corresponds to the maneuver location that minimizes the total required control effort to reach the specified observation point. This point appears in the black box. At this location, a targeting maneuver enables the vehicle to reach the final desired location.

VI. Results of the Control Analysis

The various control strategies are implemented in differing combinations for DRM 4 and DRM 5. For example, in one scenario, a nonlinear optimal controller is used for transit between t_1 and t_2 (in Figure 1) and an LQR controller is used to track the star during an observation period. Alternatively, an impulsive

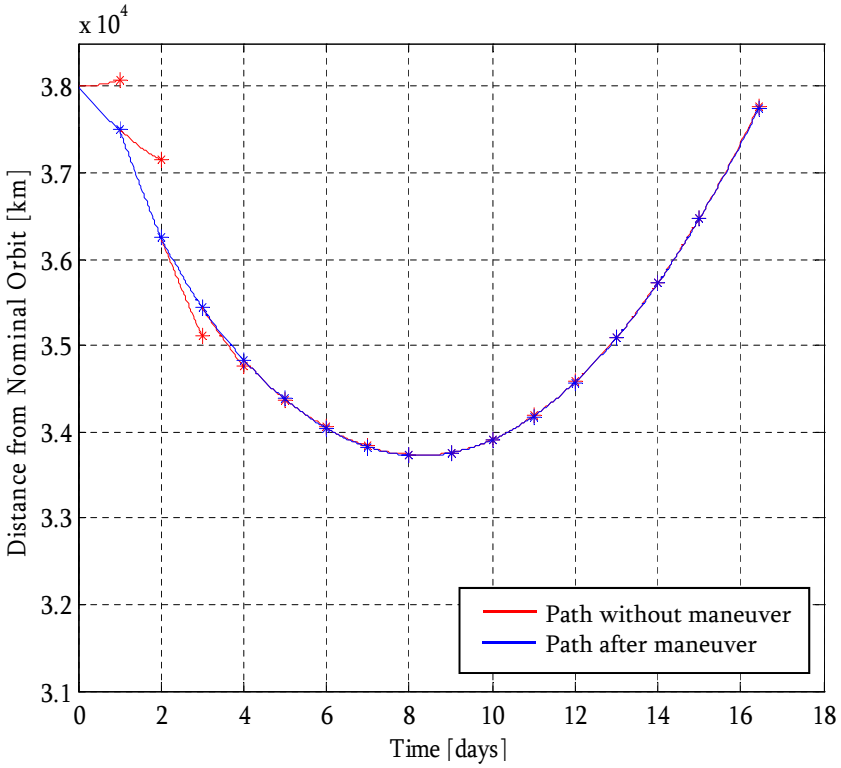

Figure 6. A Floquet control method is implemented on the TPF-O mission concept.

maneuver strategy can support the transit between t_1 and t_2, as well as between t_2 and t_3; this approach implies that no star tracking occurs during the observation period. A summary of the different scenarios and the resulting required control effort appears in Tables 3 and 4.

In Tables 3 and 4, the control cost is reflected in terms of Δv. The first column in these tables, labeled "Total ΔV" is an estimate of the control effort required for the entire mission scenario. Because each scenario contains a different number of star targets, it may be helpful to determine the average control effort used per star in the sequence. This "star cost" appears in the second column labeled "Ave. ΔV per star." In columns 3 and 4, the total control effort is divided into mission segments: transit and observation periods, respectively. Finally, the last column is a measure of only the control effort required to track the star during the observation periods. A maneuver delivers the occulter to the specified location. Then, this "star track" value is defined as the amount of control necessary to maintain the position of the occulter relative to a desired state location, to within a specified tolerance.

Notable observations emerge from the control analysis. Tables 3 and 4 both indicate that the impulsive maneuver strategy, used during the transit period, requires the least amount of control effort. The impulsive geometric "Floquet" maneuvers require the most control effort during the transit period. DRM 4 requires a significantly higher average control effort per star than DRM 5, as is apparent from column 2 in Tables 3 and 4. Upon further investigation, it is apparent that this is a result of the larger distance between the telescope and the occulter: 72,000km for DRM 4 as opposed to 38,700 km for DRM 5. As the occulter is placed further and further from the nominal telescope orbit, the control cost tends to increase. This is due, in part, to the longer distance through which the occulter must pass to create the desired angle during each observation period.

The required control at each star can also be represented graphically, as plotted in Figures 8 and 9. A notional thrust profile for DRM 4 appears in Figure 8. This profile corresponds to row 3 in Table 3: impulsive control during transit periods and LQR control during observation periods. The horizontal axis represents each star in the DRM 4 sequence. The vertical axis represents the amount of control required at a particular star in the sequence. The total required control effort for the DRM 4 mission is plotted in red. Consistent with the tables, this control effort is divided into the control required for the observation

Table 3. A comparison of control strategies for DRM 4.

Control Method	Total ΔV [km/s]	Ave. ΔV per star [m/s]	Transit ΔV [km/s]	Observation ΔV [km/s]	Star Track [m/s]
Impulsive Transit without Star Track	4.728	35.284	4.728	–	–
Impulsive Transit + Impulsive Star Track	5.783	43.157	2.795	2.947	–
Impulsive Transit + LQR Star Track	5.955	44.440	2.702	3.253	30.074
Impulsive Transit + IFL Star Track	5.966	44.522	2.704	3.263	30.166
LQR Transit + LQR Star Track	5.998	44.761	2.745	3.253	30.074
IFL Transit +IFL Star Track	6.067	45.275	2.804	3.263	30.166
NL Optimal Transit + Impulsive Star Track	5.802	43.299	2.855	2.947	–
NL Optimal Transit + LQR Star Track	6.103	45.545	2.850	3.253	30.074
NL Optimal Transit + IFL Star Track	6.111	45.604	2.848	3.263	30.166
Geometric Transit + Impulsive Star Track	6.792	50.687	3.845	2.947	–
Geometric Transit + LQR Star Track	6.804	50.776	3.551	3.253	30.166
Geometric Transit + IFL Star Track	6.811	50.828	3.548	3.263	30.166

Table 4. A comparison of control strategies for DRM 5.

Control Method	Total ΔV [km/s]	Ave. ΔV per star [m/s]	Transit ΔV [km/s]	Observation ΔV [km/s]	Star Track [m/s]
Impulsive Transit without Star Track	2.721	26.676	2.721	–	–
Impulsive Transit + Impulsive Star Track	2.899	28.422	1.506	1.392	–
Impulsive Transit + LQR Star Track	3.009	29.500	1.452	1.558	13.555
Impulsive Transit + IFL Star Track	3.013	29.539	1.451	1.561	13.581
LQR Transit + LQR Star Track	3.032	29.725	1.474	1.558	13.555
IFL Transit +IFL Star Track	3.111	30.500	1.549	1.561	13.581
NL Optimal Transit + Impulsive Star Track	2.995	29.363	1.603	1.392	–
NL Optimal Transit + LQR Star Track	3.101	30.402	1.543	1.558	13.555
NL Optimal Transit + IFL Star Track	3.104	30.431	1.543	1.561	13.581
Geometric Transit + Impulsive Star Track	3.213	31.500	1.821	1.392	–
Geometric Transit + LQR Star Track	3.298	32.333	1.740	1.558	13.555
Geometric Transit + IFL Star Track	3.302	32.373	1.741	1.561	13.581

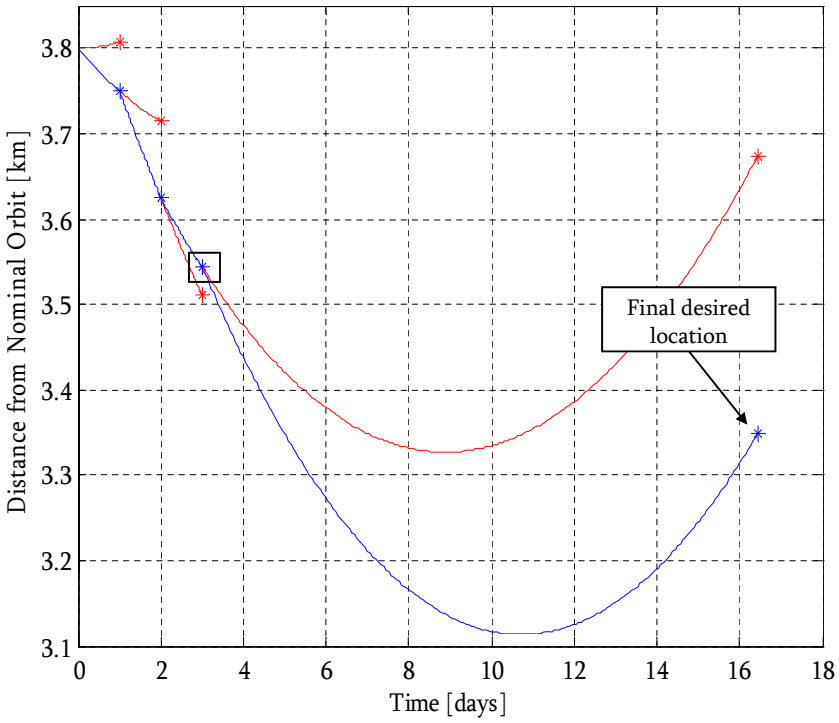

Figure 7. A Floquet control method is implemented on the TPF-O mission concept.

period and that required for the transit period, that is, the green and the cyan line, respectively. The dark blue line indicates the amount of control required if analysis is completed without CR3BP dynamics. In other words, the spacecraft are assumed to be moving in free space. It is notable that the control effort required for spacecraft moving in free space is significantly higher than that required for spacecraft moving in the CR3BP. Thus, in this mission scenario, the natural dynamics in this regime reduce the control cost of the spacecraft maneuvers. Similarly, Figure 9 illustrates a notional thrust profile for DRM 5. This profile corresponds to row 9 in Table 4: nonlinear optimal control during transit periods and input-state feedback linearization during observation periods. Again, the required control for a spacecraft formation moving in free space is significantly higher than for a formation moving in the CR3BP.

VII. Effectiveness of the Control Methods on Mission Goals

During the transit period, no requirements exist on the position and velocity of the spacecraft formation to facilitate imaging. During the observation, however, the occulter must remain within 100 km of the specified path in the radial direction and within 10 m of the specified path in the transverse direction. Three different control methods are evaluated for use during the observation period: impulsive control, input-state feedback linearization, and LQR control. When impulsive control is employed during the observation period, generally, the mission requirements are not met. However, when either input-state feedback linearization or LQR control are applied, weighting matrices can be selected such that position errors are within required tolerances.

An example of the required control effort and state error response in the transverse direction, during a single sample observation period of the TPF-O mission, appears in Figure 10. The control effort in the first column of Figure 10 corresponds to the first observation period in the star sequence for DRM 5. The weighting matrices, Q_z and R_z, are defined such that the state error is just within the defined mission tolerances. The required control in the transverse direction is plotted as a function of time for three different control methods. In the second column of Figure 10, the state error in the transverse direction for the corresponding control method is displayed.

The typical required control effort and the state error response in the corresponding radial direction are

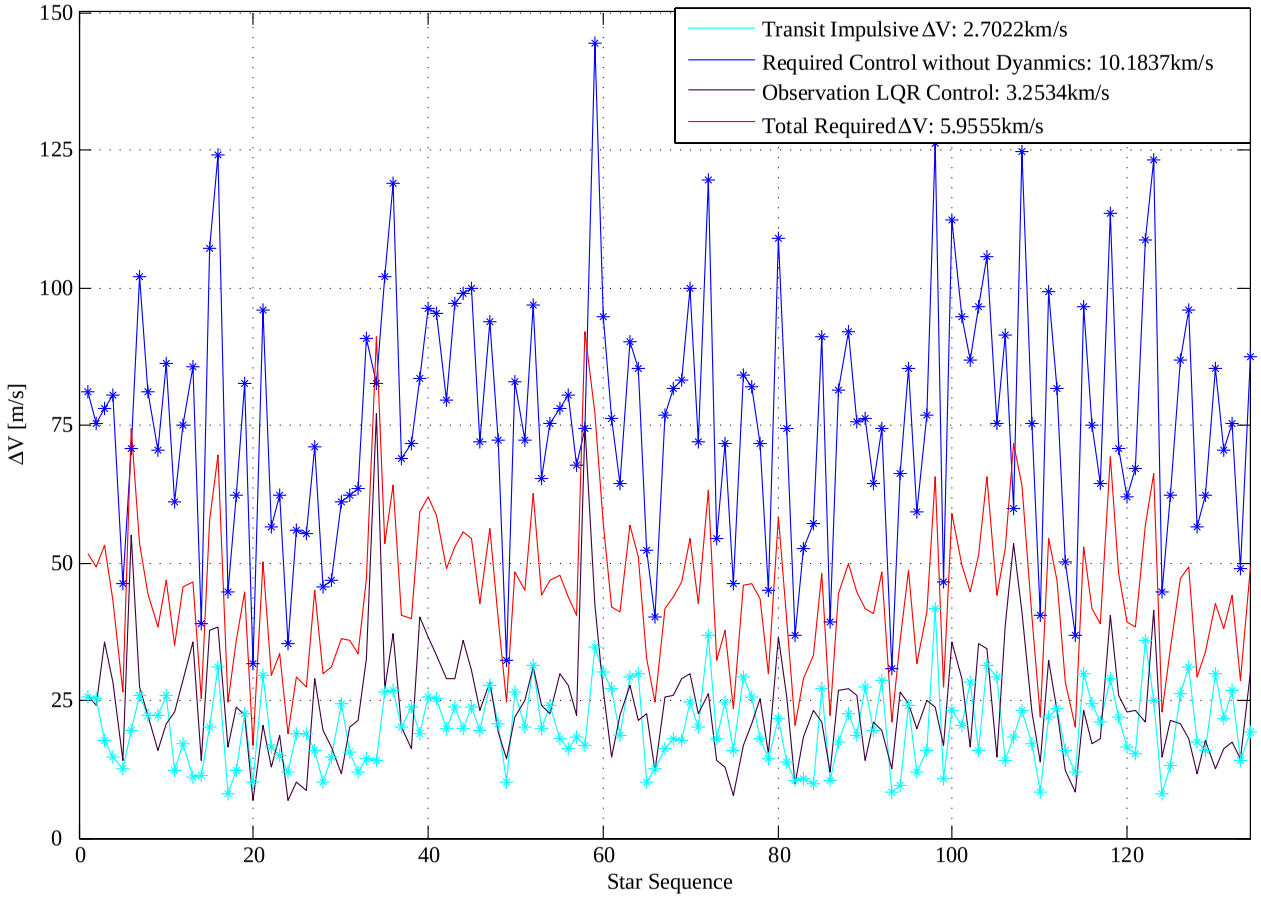

Figure 8. A notional thrust profile for the TPF-O Design Reference Mission 4: impulsive control during transit periods and LQR control during observation periods.

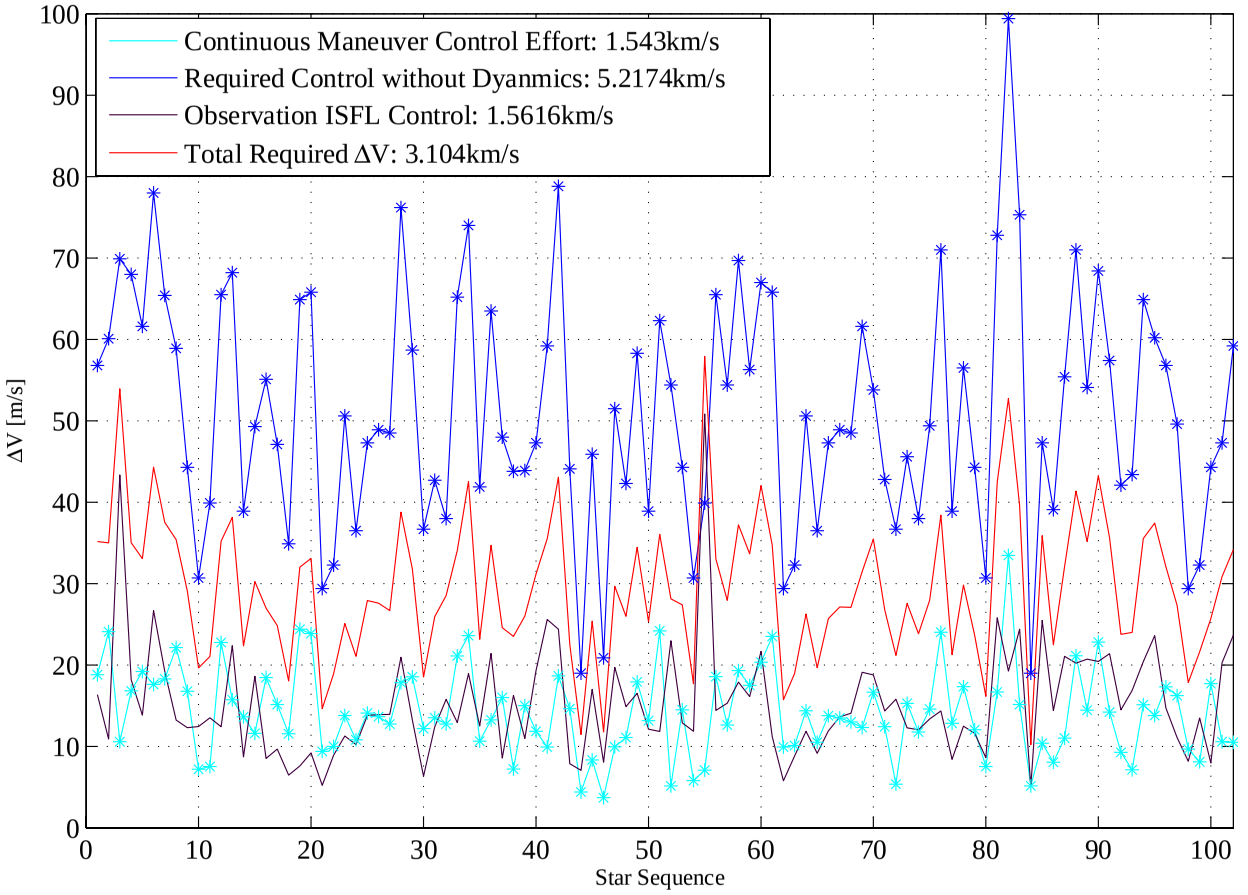

Figure 9. A notional thrust profile for TPF-O design reference mission 5 utilizes nonlinear optimal control during transit periods and input-state feedback linearization control during observation periods.

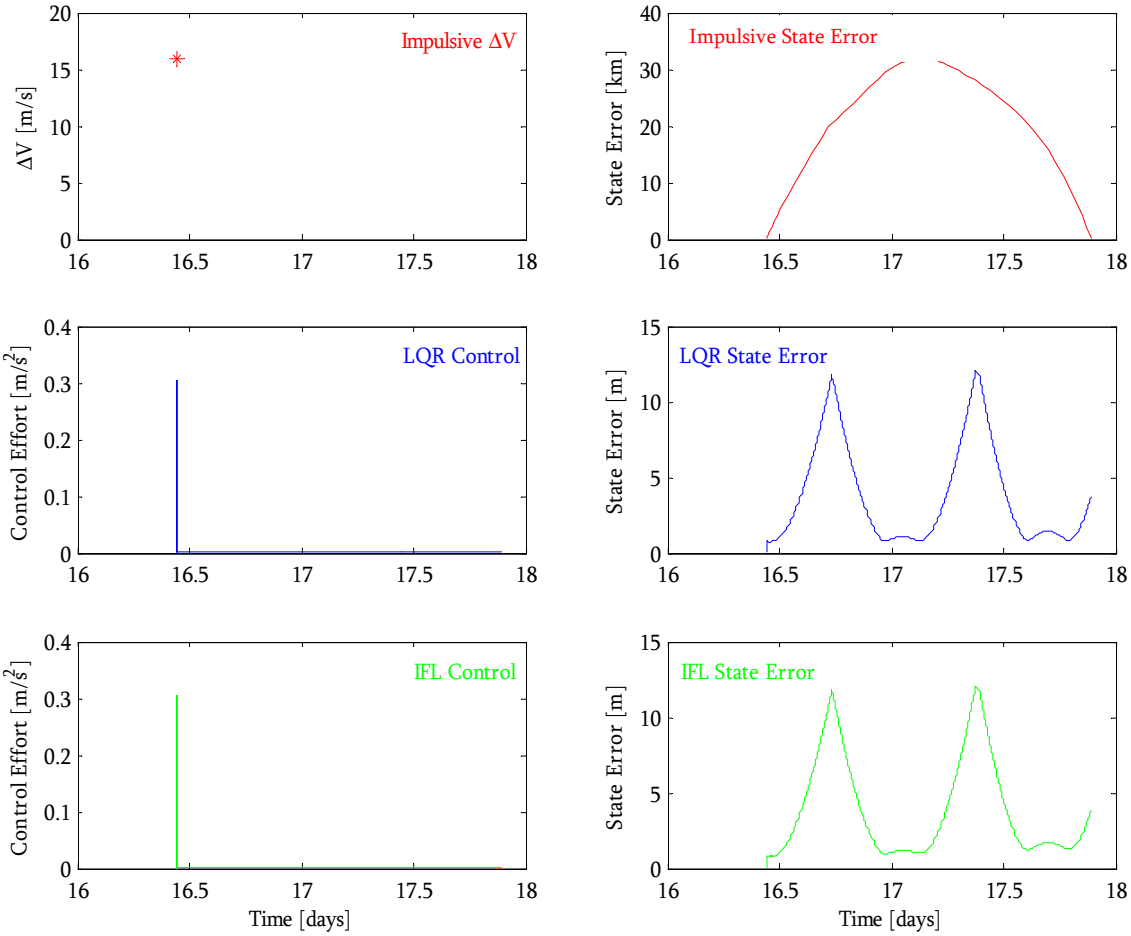

Figure 10. An example of error in the transverse state is demonstrated to be within mission-defined tolerance for TPF-O.

plotted in Figure 11. Because the position tolerance in the radial direction is much more lax, the state error response is much higher in magnitude. This, again, results in part from the selection of Q_z and R_z. In the first column of the figure, the required control in the radial direction appears as a function of time for three different control methods applied to star tracking. The second column in the plot displays the state error in the radial direction for the corresponding control method.

Preliminary results of error analysis performed on DRM 4 via LQG, as described in Section V.B, appear in Table 5. The first two columns of Table 5 represent the Gaussian mean error added to the state measurement in both position and velocity. In other words, this is the average and median error included in the analysis. The third column is the average increase in required control cost, given the error in the first two columns. The control cost (δv) is calculated as the average integral of the control history (in m/s^2) determined via the continuous LQG controller. From Table 5, it is obvious that larger error in the state estimate results in higher values of control that is necessary to meet the same mission specifications. Also, error in the velocity component of the state results in a significantly larger increase in required control than error in position. Thus, the system is more sensitive to error in velocity. As the measurement error becomes increasingly large, the control cost may become prohibitively high for a realistic successful mission.

Finally, an example of the path, including both the occulter and telescope spacecraft, appears in Figure 12. This trajectory corresponds to line 3 in Table 4 and line 2 in Table 5. The trajectory of the telescope appears in blue, following the nominal Lissajous orbit. The occulter path is both red and cyan, indicating the transit and observation periods, respectively. Thus, each red star on the trajectory indicates a maneuver point, or a point where the occulter spacecraft performs an impulsive maneuver. The occulter then coasts until it reaches alignment with a desired star. This coasting period is indicated by a red line. The point at which the occulter telescope array is aligned with a desired star is denoted by a cyan star. After reaching

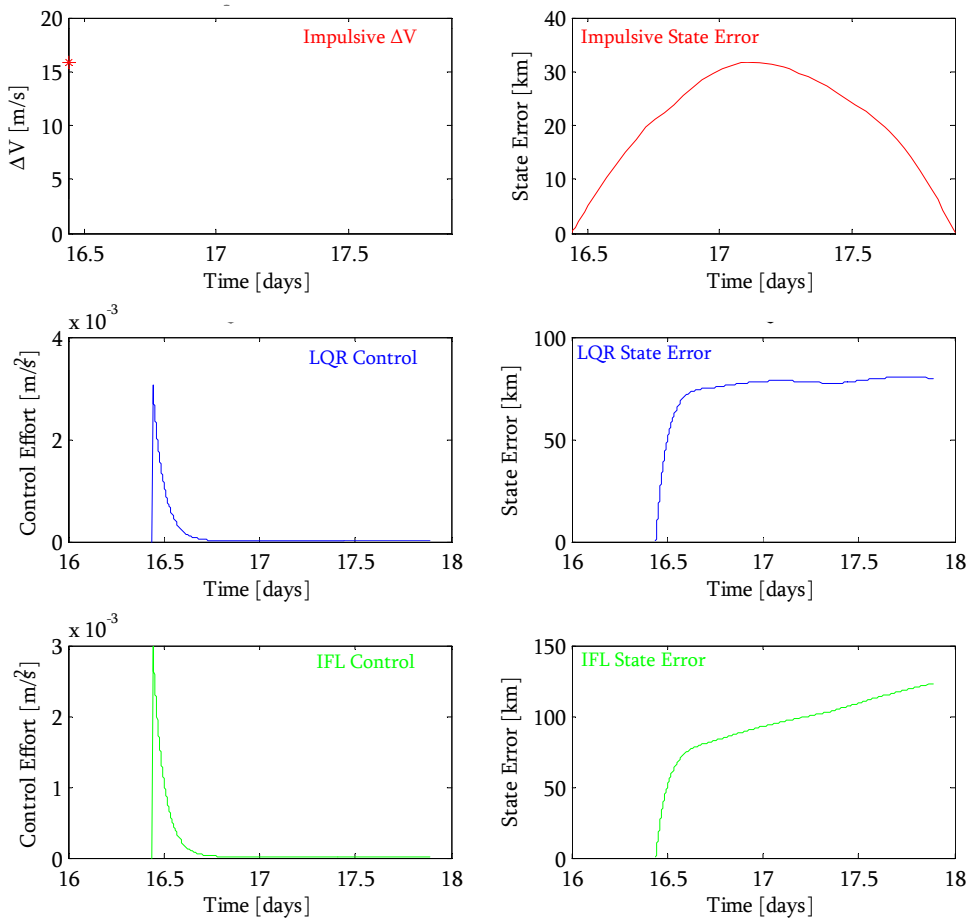

Figure 11. An example of error in the radial state is demonstrated to be within the mission-defined tolerance for TPF-O.

Table 5. Preliminary error analysis for the DRM 4 mission.

Gaussian Mean Error in State Measurement		Average Increase in Required Δv
Position [m]	Velocity [mm/s]	[m/s]
0	0	0
5	5	14
10	10	21
5	100	30
10	1000	96
100	5	25
1000	10	32

alignment with a star, the continuous LQR control is applied during the entire observation period. During this time, the spacecraft path is indicated by a cyan line.

VIII. Concluding Remarks

This analysis represents a comparison of various control strategies for the TPF-O mission concept. These strategies include LQR control, input-state feedback linearization, impulsive control, nonlinear optimal control, and geometric control. Error inclusion as well as estimation filters via LQG analysis are incorporated. The different control methods are evaluated for efficacy, given specific constraints on the motion of the occulter spacecraft. The software package that produced these results may be used to evaluate future design reference missions.

The TPF-O DRM 4 and DRM 5 mission concepts are feasible, i.e., required mission tolerances can be maintained with limited error inclusion. However, not all control strategies are capable of meeting mission requirements on the state of the occulter spacecraft. The control strategy that meets all mission requirements while using the smallest amount of control is a combination of LQR and impulsive control methods. The LQR

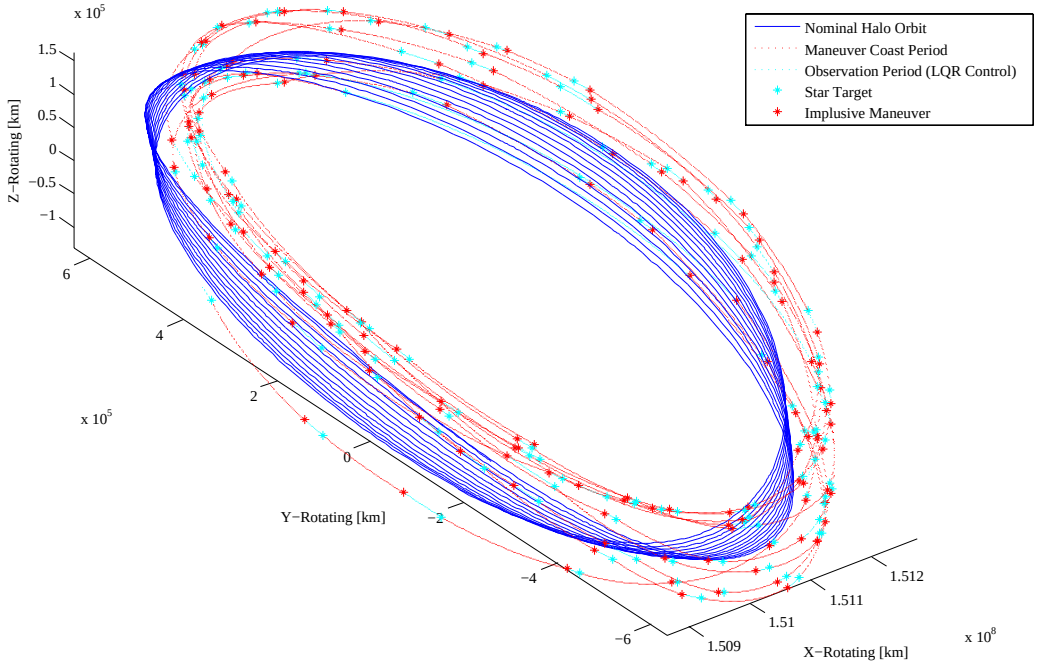

Figure 12. The telescope moves along a nominal Lissajous orbit, while the occulter performs maneuvers near the orbit to track different stars.

control strategy is implemented during the observation period and the impulsive maneuvers are employed during the transit period. Using this control strategy, the total mission $\Delta\bar{v}$ is approximately 6 km/s for DRM 4 and 3 km/s for DRM 5. It is noted that the nominal distance between the occulter and telescope spacecraft are 72,000 km and 37,800 km for DRM4 and DRM5, respectively.

For two TPF-O design references missions, it is observed that inclusion of the natural dynamics in the model reduces the control cost for maneuvers. Such a result highlights the importance of including dynamics in mission control analysis in multi-body regimes. If all forces acting on the spacecraft were to be approximated as simply the force due to the spacecraft thrusters (moving in "deep space"), higher control requirements would be predicted.

A reduction in overall mission control cost may be accomplished in two ways. First, control savings emerge for a mission designed such that the occulter is closer, rather than farther, from the telescope spacecraft. As the distance between the occulter and telescope spacecraft is increased, the required control for maneuvers increases. This may be due, in part, to the advantageous natural dynamics near the nominal Lissajous orbit; the dynamic regime changes as the occulter moves farther from the nominal orbit. Of course, the distance between the spacecraft may not be flexible. Second, the order and the location of stars in a sequence could affect the necessary control effort. If these stars could be based, in part, on the level of control effort required, the cost could be reduced. However, mission design scenarios may stipulate a specific star sequence to maximize scientific results.

IX. Acknowledgements

The authors would like to thank Dave Folta, Conrad Schiff, and the TPF-O working group at NASA Goddard Space Flight Center for providing information and guidance for the current study. This work was performed at Purdue University with support from NASA Goddard Space Flight Center under contract numbers NCC50-727 and NNG04GP69G. Support was also provided from Purdue University via the Bilsland Dissertation Fellowship.

References

[1]Schultz, A. B., Schroeder, D. J., Jordan, I., Bruhweiler, F., DiSanti, M. A., Hart, H. M., Hamilton, F. C., Hershey, J., Kochte, M., Miskey, C. L., Cheng, K. P., Rodrigue, M., Johnson, B., and Fadali, M. S., "Imaging Planets About OtherStars with UMBRAS, an Infrared Spaceborne Sensing VII," *Proceedings of SPIE*, Vol. 3759, No. 29, 1999.

[2]Schultz, A. B., Jordan, I., Hart, H. M., Bruhweiler, F., Fraquelli, D. A., Hamilton, F. C., Hershey, J., Kochte, M., DiSanti, M. A., Miskey, C. L., Cheng, K. P., Rodrigue, M., Johnson, B., and Fadali, M. S., "Imaging Planets About Other Stars with UMBRAS II, in Infrared Spaceborne Sensing VIII," Vol. 4131, No. 3, 2000.

[3]Cash, W., "Detection of Earth-Like Planets Around Nearby Stars Using a Petal-Shaped Occulter," Vol. 442, 2006.

[4]Danner, R., Unwin, S., and Allen, R. J., "SIM: Space Interferometry Mission: Taking Measure of the Universe," Tech. rep., National Aeronautics and Space Administration, Washington, DC, 1999.

[5]Beichman, C. A., "Terrestrial Planet Finder: The Search for Life-Bearing Planets Around Other Stars," *Proceedings of SPIE*, Vol. 3350, No. 719, 1998.

[6]Heap, S. R., "The Terrestrial Planet Finder-Occulter Science Program," *Proceedings of SPIE*, Vol. 6687, September 20 1998.

[7]Lo, M., "External Occulter Trajectory Study," Jet Propulsion Laboratory PowerPoint Presentation.

[8]Vanderbei, R., Kasdin, N. J., and Cady, E., "Optimal Occulter Design for Finding Extrasolar Planets," astroph/0704.3488, 2007.

[9]Leitner, J., "Formation Flying System Design for a Planet-Finding Telescope Occulter System," *Proceedings of SPIE*, Vol. 6687, August 2007.

[10]Millard, L. D. and Howell, K. C., "Optimal Re-Configuration Maneuvers for Imaging Arrays in Multi-Body Regimes," *IAF Conference Proceedings*, Hyderabad, India, September 24–28 2007.

[11]Howell, K. C. and Marchand, B. G., "Control Strategies for Formation Flight in the Vicinity of the Libration Points," *AAS/AIAA Space Flight Mechanics Meeting*, Ponce, Puerto Rico, February 9–13 2003, AAS Paper No. 03-113.

[12]Perko, L., *Differential Equations of Dynamical Systems*, Springer Verlag, New York, 2nd ed., 1996.

[13]Patterson, C. E., *Representations of Invariant Manifolds for Applications in System-to-System Transfer Design*, Master's thesis, Purdue University, West Lafayette, IN, May 2005.

[14]Gómez, G., Howell, K., Masdemont, J., and Simó, C., "Station-keeping Strategies for Translunar Libration Point Orbits," *Advances in Astronautical Sciences*, Vol. 99, No. 2, 1998, pp. 949–967.

[15]Howell, K. C. and Keeter, T. M., "Station-Keeping Strategies for Libration Point Orbits: Target Point and Floquet Mode Approaches," *AAS/AIAA Spaceflight Mechanics Meeting*, Albuquerque, New Mexico, February 13-16 1995.

[16]Marchand, B. G. and Howell, K. C., "Aspherical Formations Near the Libration Points in the Sun-Earth/Moon Ephemeris System," *AIAA/AAS Spce Flight Mechanics Conference*, Maui, Hawaii, February 8-11 2004, AAS Paper 04-157.